9. M. R. Showalter, J. N. Cuzzi, S. M. Larson, *Icarus* **94**, 451 (1991).
10. M. R. Showalter and J. N. Cuzzi, *ibid.* **103**, 124 (1993).
11. M. R. Showalter, *Bull. Am. Astron. Soc.* **23**, 1178 (1991).
12. ———, *ibid.* **25**, 1109 (1993).
13. C. C. Porco, *Science* **253**, 995 (1991).
14. M. E. Ockert, J. N. Cuzzi, C. C. Porco, T. V. Johnson, *J. Geophys. Res.* **92**, 14969 (1987).
15. B. A. Smith *et al.*, *Science* **212**, 163 (1981).
16. M. R. Showalter, *Nature* **351**, 709 (1991).
17. P. Goldreich, S. Tremaine, N. Borderies, *Astron. J.* **92**, 490 (1986).
18. B. Sicardy, *Icarus* **89**, 197 (1991).
19. P. Thomas, C. Weitz, J. Veverka, *ibid.* **81**, 92 (1989).
20. P.-Y. Longaretti, *ibid.* **82**, 281 (1989).
21. C. C. Porco, P. D. Nicholson, J. N. Cuzzi, J. J. Lissauer, L. W. Esposito, in *Neptune and Triton*, D. P. Cruikshank, Ed. (Univ. of Arizona Press, Tucson, in press).
22. The processing behind the profiles involves (i) correcting the camera orientation on the basis of the observed locations of background stars (and allowing for stellar aberration in the frame of the planet); (ii) masking out all invalid pixels, such as those containing stars, satellites, blemishes in the camera vidicon, or reseau markings; (iii) converting the image to a one-dimensional profile by averaging together all unmasked pixels falling at the same radius but different longitudes; and (iv) removing residual background variations by fitting a low-order polynomial to the samples outside the ring's radial limits and subtracting it. These procedures are described elsewhere (*9, 10*). Note that step (iii) substantially increases the detectability of faint rings; a narrow ring typically occupies ~800 pixels in a Voyager image, so this averaging improves the signal-to-noise ratio by a factor of $\sqrt{800} \approx 30$.
23. I thank the Voyager Imaging and PPS teams and the Planetary Data System Imaging Node for providing the data. I am indebted to A. Dobrovolskis, L. Dones, R. French, B. Sicardy, and two anonymous referees for helpful comments and criticisms. This work was supported by the National Aeronautical and Space Administration (NASA) Planetary Geology and Geophysics program and by NASA Ames under grant NAG2-673.

26 July 1994; accepted 25 October 1994

Energy Dependence of Abstractive Versus Dissociative Chemisorption of Fluorine Molecules on the Silicon (111)-(7×7) Surface

John A. Jensen, Chun Yan, Andrew C. Kummel*

Scanning tunneling microscopy and monoenergetic molecular beams have been used to obtain real-space atomic images of the competition between abstractive and dissociative chemisorption. The size distribution of Si–F adsorbates on the Si(111)-(7×7) surface was examined as a function of the incident translational energy of the F_2 molecules. For F_2 molecules with 0.03 electron volt of incident energy, the dominant adsorbate sites were isolated Si–F species. As an F_2 molecule with low translational energy collides with the surface, abstraction occurs and only one of the F atoms chemisorbs; the other is ejected into the gas phase. For F_2 molecules with 0.27 electron volt of incident energy, many adjacent Si–F adsorbates (dimer sites) were observed because F_2 molecules with high translational energy collide with the surface and chemisorb dissociatively so that both F atoms react to form adjacent Si–F adsorbates. For halogens with very high incident energy (0.5–electron volt Br_2), dissociative chemisorption is the dominant adsorption mechanism and dimer sites account for nearly all adsorbates.

The chemisorption of F_2 is often the first step in the dry etching of Si. For most molecules, chemisorption on surfaces occurs either through a physisorbed precursor state or by direct chemisorption (*1*). Dissociative chemisorption is a common gas-surface process in which an incident molecule collides with the surface and breaks apart to form two or more chemisorbates. For dissociative chemisorption of F_2 on Si, direct chemisorption is so highly exothermic that a distinct mechanism can occur. In abstractive chemisorption, as an incident F_2 collides with the surface, one F atom is chemisorbed onto a Si atom and the terminal F atom is ejected into the gas phase. Molecular beam scattering experiments by Ceyer and coworkers (*2*) have demonstrated the existence of abstractive chemisorption for F_2 on the Si(100)-(2×1) surface; to our knowledge, this is the only experimental report of abstractive chemisorption of any molecule onto a surface. Molecular dynamics simulations by Carter *et al.* (*3*) have shown that this abstraction mechanism is most efficient at low translational energy, whereas dissociative chemisorption is most efficient at high translational energies. They have also shown that the reaction of F_2 with the Si(100)-(2×1) surface always proceeds in a stepwise fashion, the first step being the chemisorption of one F atom and the cleavage of the F–F bond. The escape or adsorption of the second F atom is the difference between abstractive and dissociative chemisorption.

In this report, we present atomic-resolution scanning tunneling microscopy (STM) images of the Si(111)-(7×7) surface after chemisorption of F_2 molecules with low and high translational energies. These images allow direct observation of how the probability for abstraction varies with the incident translational energy of F_2 in the limit of zero coverage. We show that for F_2 molecules with low incident translational energy, nearly all chemisorption sites are Si–F monomers, that is, isolated single sites formed through abstractive chemisorption. We also show that for F_2 molecules with higher incident translational energy, many more chemisorption sites are dimers, that is, two nearest neighbor Si–F sites formed through dissociative chemisorption. Finally, for Br_2 molecules with very high incident translational energy, dissociative chemisorption accounts for essentially all adsorption because single-site adsorbates are almost absent. Our experiments show that the competition between abstractive and dissociative chemisorption is mediated by the incident translational energy and momentum of the molecule.

Both molecular beam techniques and STM are required to examine the initial stages of F_2 adsorption onto the Si(111)-(7×7) surface. The supersonic expansion of the halogen–carrier gas mixture provides a source of halogen molecules with a very narrow translational energy distribution ($\Delta E/E \leq 2\%$) as well as a low rotational temperature (~4 K). By changing the mixture ratio or mass of the carrier gas, it is possible to vary the translational energy of the halogen without changing the rotational or vibrational temperature of the molecules. The STM allows us to examine the resulting adsorbate structures with atomic resolution.

Earlier experiments and calculations (*2, 3*) characterizing the abstraction mechanism were carried out on the dimer row Si(100)-(2×1) surface. In our study we used the Si(111)-(7×7) surface. The structure of the Si(111)-(7×7) unit cell is well known (*4*) (Fig. 1). Only the adatoms (first layer) and those rest atoms (second layer) with dangling bonds are shown in Fig. 1; these are the surface atoms that do not have complete coordination of four neighboring Si atoms and thus have localized electron density that is centered along the missing bond axis. This localized electron density is termed a dangling bond. Empty-state STM images show only the adatom dangling bonds (the 12 uppermost Si atoms shown as open circles inside the border in Fig. 1). Empty-state images do not show the rest atom dangling bonds located one atomic layer below (the six atoms shown as crossed circles in Fig. 1). It has been shown experimentally (*5*) and theoretically (*6*) that each adatom dangling bond has an occupancy of approximately one-half an elec-

Department of Chemistry, 0358, University of California, San Diego, 9500 Gilman Drive, La Jolla, CA 92093, USA.
*To whom correspondence should be addressed.

tron, whereas each rest atom dangling bond has two electrons. In the limit of zero coverage, it is assumed that all reactions of F_2 will occur at the adatoms (surface-bound radicals) and not at the rest atoms (surface-bound lone pairs) (*7*).

Halogen adsorption onto an Si adatom will create both a Si–X σ bonding state (filled, energy below the Fermi level) and a σ^* antibonding state (empty, energy above the Fermi level). Empty-state STM images are relatively low bias (<1 V) show the Si–X as a dark sites, just as a missing adatom would appear because the tunneling electrons are insufficiently energetic to access the empty antibonding orbital (*7*). The Si–F bond strength is 6.1 to 6.4 eV (*8*), and therefore a very high bias (>4 V) would be required to image the Si–F σ^* state. Unfortunately, at STM tip-surface biases above 4 V, atomic resolution is lost and other deleterious effects particular to the F_2/Si(111)-(7×7) system are observed.

Our STM images are empty-state images obtained in the constant-current mode at room temperature with scan rates of 0.5 or 0.75 Hz, a very low tip-surface bias (V_{tip} = −0.2 to −1 V), and low tunneling current ($I_t \approx 0.3$ nA). Coverages are reported here in terms of the percentages of adatoms that have reacted to form monofluorides (1.92×10^{14} adatoms per square centimeter). The F_2 monolayer coverage on the Si(111)-(7×7) surface has been measured (*9*) at 1.58×10^{15} F atoms per square centimeter; therefore, 3 to 4% reacted adatoms corresponds to 0.4 to 0.5% of a monolayer. Examination of our clean Si(111)-(7×7) surfaces shows that our average initial defect density was 0.5% missing adatoms. These defects consist almost exclusively of isolated single vacancies. Under our imaging conditions (low tip-surface bias), a dark adatom site is either an initial adatom vacancy or a chemisorbed F atom. Because of the indistinguishability of monofluorides and initial vacancies, we examined 500 to 550 unit cells for adsorbate size distributions to ensure that fluctuations in the density of vacancies would not dominate the analysis.

Representative scans of the Si(111)-(7×7) surface dosed with F_2 at incident translational energies of 0.03 eV (10% in Kr) and 0.27 eV (5% in He) at total coverages of 3.3 and 3.5% reacted adatoms are shown in Fig. 2, A and B, respectively. The images were analyzed to obtain the number of nearest Si–F neighbors. The translational energies of the carrier gases Kr and He are 0.07 and 0.05 eV, respectively. These energies are insufficient to cause collision-induced desorption of fluorinated surface species (*10*). In Fig. 3A, the percentage of the total coverage contained in adsorbates of a given size is plotted against the adsorbate size given as the number of neighboring monofluorinated adatoms; data are presented for three translational energies, 0.03, 0.09, and 0.27 eV. As the translational energy is increased, there is a clear shift away from single-site adsorption (abstraction) toward double-site adsorption (dissociative chemisorption). Therefore, the adsorption probability of the second F atom increases as the F_2 molecule is driven farther into the surface by increasing incident translational energy and momentum. For F_2 molecules with an incident translational energy of 0.03 eV, ~70% of the total reacted adatoms are isolated single fluorinated adatoms, whereas only 15% are in the form of two neighboring reacted adatoms (dimer). In contrast, for F_2 molecules with an incident translational energy of 0.27 eV, only 45% of the total reacted adatoms are single reacted adatoms, whereas 30% are in the form of two neighboring reacted adatoms. The number of dimer sites has doubled with the increased incident translational energy. There is a ~10% probability that two separate abstractive adsorptions will occur on adjacent sites for a lattice with six or seven nearest neighbors and a coverage of 3%. Therefore, we cannot attribute all double adsorption sites to dissociative chemisorption even at these low coverages.

For an extreme comparison, we examined the chemisorption of Br_2 with a translational energy of 0.5 eV on the Si(111)-(7×7) surface. Because of the relatively small mass of fluorine, it is difficult to obtain translational energies greater than 0.27 eV (5% F_2 in He). Because Br_2 has a mass more than four times as great as F_2, a 0.5-eV beam of Br_2 is easily prepared (~13% Br_2 in He). The amount of abstraction should be considerably less in the Br_2/Si(111) system than in the F_2/Si(111) system because of the increased momentum driving the second halogen atom into the surface. We did not examine Br_2 molecules with lower translational energy because of the presence of large Si–Br islands, which are the result of precursor-mediated chemisorption (*1*), a channel that is absent for F_2

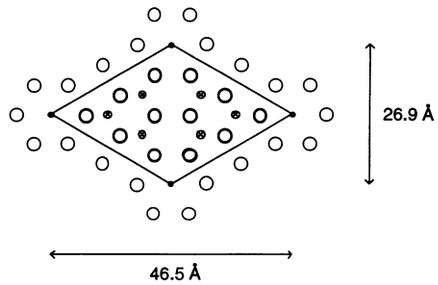

Fig. 1. Schematic of the Si(111)-(7×7) unit cell (one unit cell is within the borders). Open circles (12 per unit cell) represent the adatoms, the uppermost atomic layer. Crossed circles (6 per unit cell) represent the rest atoms with dangling bonds that are located one atomic layer below the adatoms. The small black circles (1 per unit cell) represent the corner-hole rest atoms and are two atomic layers below the adatoms.

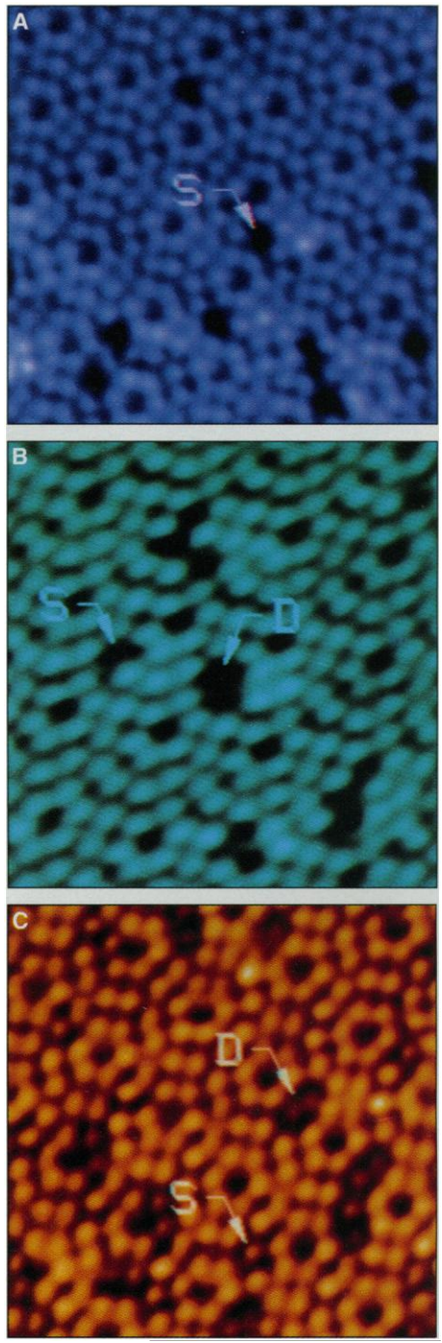

Fig. 2. Constant-current, empty-state STM images of Si(111)-(7×7) after exposure to (**A**) 0.03-eV F_2 with a total coverage of 3.2% reacted adatoms; (**B**) 0.27-eV F_2 with a total coverage of 3.5% reacted adatoms; and (**C**) 0.5-eV Br_2 with a total coverage of 5.5% reacted adatoms. Imaging biases are 0.8, 1.0, and 0.6 V, respectively. The Si–Br σ^* state is imaged at a relatively low bias; S, single site; D, dimer site. Single sites dominate for 0.03-eV F_2 (A), whereas dimers dominate adsorption for 0.5-eV Br_2 (C). Images are uncorrected for thermal drift.

chemisorption. This chemisorption channel dominates at low translational energies, and the resulting islands complicate the size distribution analysis.

A representative scan of the Si(111)-(7×7) surface exposed to a 0.5-eV beam of Br_2 is shown in Fig. 2C. Because the Si–Br bond strength is only 3 to 4 eV (*11*), a relatively low bias is required to access the Si–Br σ* state and thereby distinguish it from an initial vacancy (*12*). The bromine coverage is 5.5%, and the defect (vacancy) density is 0.4%. Double-site adsorption dominates the coverage. The resulting histogram showing the coverage versus size is shown in Fig. 3B. Initial defects are not included in the analysis. Although the coverage is higher, comparison to the 0.03-eV F_2 size distribution (Fig. 3A) shows a drastic shift from abstraction (single-site) to dissociative chemisorption (double-site). The increased number of even-sized adsorbates (size 2, 4, and 6 in Fig. 3B) further demonstrates that dissociative chemisorption onto neighboring adatoms is the dominant adsorption process. However, the presence of isolated monobromides and odd-sized adsorbates shows that abstraction is still occurring, but at a much lower probability.

In order to quantify the relative amounts of abstraction or dissociative chemisorption, we have used a simple Monte Carlo model to mimic the size distribution as the probability of single- and double-site adsorption is varied. The model is a square lattice with eight nearest neighbors onto which one or two neighboring points are randomly placed until the desired coverage is reached. We also examined a square lattice with six nearest neighbors and with no connectivity along one diagonal, but it showed negligible difference from the model with eight nearest neighbors. This model is not meant to simulate the actual adsorption process, but it is used merely to relate the probability of abstraction to the experimental coverage versus size distributions. We have assumed that dissociative chemisorption occurs only on nearest neighbors, which excludes the possibility of "long-range" dissociative chemisorption producing two isolated Si–F pairs. Such long-range dissociative chemisorption has been reported in the O_2/Al(111) system (*13*) but is not theoretically supported in the F_2/Si(100)-(2×1) system (*3*). In addition, the extremely large corrugation of the (7×7) surface and the high Si–F bond strength disfavor the migration of atomic F.

The model's size versus the coverage data for 100% single-site adsorption is shown in Fig. 4A together with the 0.03-eV F_2 data. Even at coverage as low as 3.2%, there are adsorbates of size 2 and greater formed by two or more separate single-site events occurring on nearest neighbor sites. Comparison to the 0.03-eV F_2 coverage distribution shows that chemisorption occurs exclusively through abstraction at this translational energy. The model's calculation for 75% single-site and 25% double-site adsorption with 0.5% initial defects is shown in Fig. 4B. Single sites are placed on the model's lattice to a coverage of 0.5% to approximate the initial defects, and then single (75% probability) and double (25% probability) sites are randomly placed until a coverage of 3.5% is reached. These data reproduce the 0.27-eV F_2 distribution quite well and allow an estimation of 75% abstraction at this translational energy. For the 0.5-eV Br_2 data (Fig. 4C), 30% single-site and 70% double-site adsorption with a final coverage of 5.5% (no initial defects) provides the best agreement with the experimental data, giving an estimated level of abstraction of 30% for this system. Therefore, the abstraction mechanism, first identified for F_2 on Si(100)-(2×1) by Ceyer and co-workers (*2*), is not unique to F_2 chemisorption on silicon surfaces but may be present in all halogen-semiconductor systems.

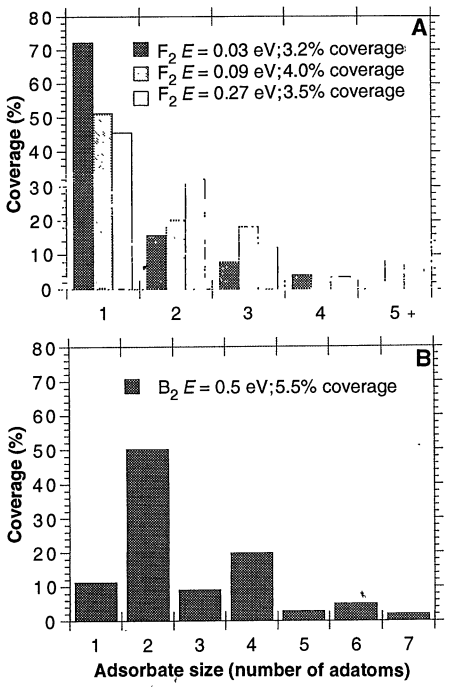

Fig. 3. Histograms of the coverage (in percent of total) versus adsorbate size (given in terms of the number of adatoms) for (**A**) F_2 + Si(111)-(7×7) and (**B**) Br_2 + Si(111)-(7×7). A total of 505, 520, and 540 unit cells were examined for F_2 at translation energies of 0.03, 0.09, and 0.27 eV, respectively; 547 unit cells were examined for Br_2 at 0.5 eV. The coverage represented by any one adsorbate size varied by ±5% relative to the total coverage in consecutive experiments. This variation is due to uncertainties in the initial level of defects (adatom vacancies) and variations in total coverage (~0.5%).

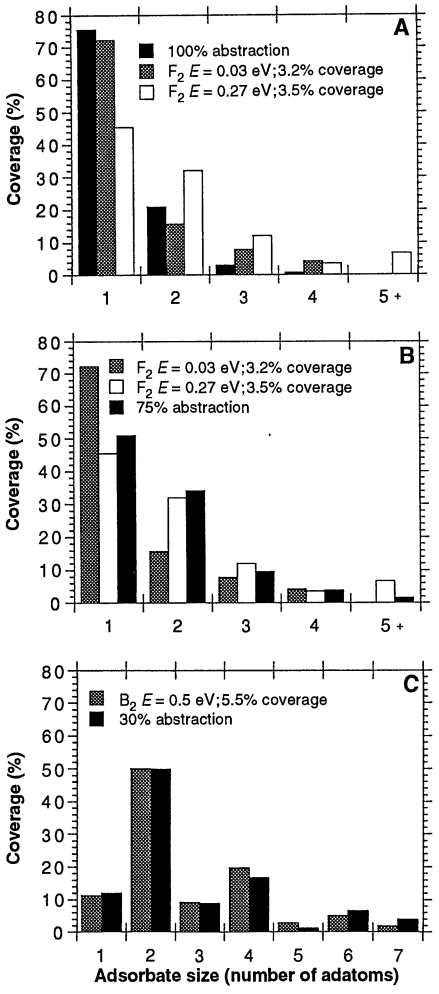

Fig. 4. Histograms of simulated coverage versus adsorbate size. Experimental data are included for comparison: (**A**) F_2 + Si(100)-(7×7) 100% single-site adsorption (abstraction) (eight nearest neighbors) with 3.2% coverage compared to the 0.03-eV F_2 data; (**B**) F_2 + Si(100)-(7×7) 75% single-site and 25% double-site adsorption (dissociative chemisorption) with 3.5% coverage and 0.5% initial defects compared to the 0.27-eV F_2 data; (**C**) Br_2 + Si(100)-(7×7) 30% single-site and 70% double-site adsorption with 5.5% coverage and 0.0% initial defects compared to the 0.5-eV Br_2 data.

REFERENCES AND NOTES

1. For a pertinent example, see H. C. Flaum, J. D. J. Sullivan, A. C. Kummel, *J. Phys. Chem.* **98**, 1719 (1994), and references therein.
2. Y. L. Li *et al.* (review by M. L. Yu and L. A. DeLouise), *Surf. Sci. Rep.* **19**, 363 (1994); J. J. Yang, D. P. Pullman, Y. L. Li, D. Gosalvez, A. A. Tsekouras, S. T. Ceyer, *Abstr. Pap. Am. Chem. Soc.* **205**, C2 (1993).
3. L. E. Carter, S. Khodabandeh, P. C. Weakliem, E. A. Carter, *J. Chem. Phys.* **100**, 2277 (1994).
4. G. Binnig *et al.*, *Phys. Rev. Lett.* **50**, 120 (1983); K. Takayanagi, Y. Tanishiro, S. Takahashi, M. Takahashi, *Surf. Sci.* **164**, 367 (1985).
5. J. E. Demuth, B. N. J. Persson, A. J. Schell-Sorokin, *Phys. Rev. Lett.* **51**, 2214 (1983); F. J. Himpsel and Th. Fauster, *J. Vac. Sci. Technol. A* **2**, 815 (1984); R. J. Hamers, R. M. Tromp, J. E. Demuth, *Phys. Rev. Lett.* **56**, 1972 (1986); Ph. Avouris and R. Wolkow, *Phys. Rev. B* **39**, 5091 (1989).

6. J. E. Northrup, *Phys. Rev. Lett.* **57**, 154 (1986).
7. For an analogy with Cl_2/Si(111)-(7×7), see J. J. Boland and J. S. Villarrubia, *Phys. Rev. B* **41**, 9865 (1991).
8. C. J. Wu and E. A. Carter, *J. Am. Chem. Soc.* **113**, 9061 (1991); *Phys. Rev. B* **45**, 9065 (1992).
9. F. R. McFreely, J. F. Morar, N. D. Shinn, G. Landgren, F. J. Himpsel, *Phys. Rev. B* **30**, 764 (1984).
10. A. Szabó, P. D. Farrall, T. Engel, *J. Appl. Phys.* **75**, 3623 (1994).
11. Estimated from the bond strength of the diatomic BrSi.
12. M. Chander, Y. Z. Li, D. Rioux, J. H. Weaver, *Phys. Rev. Lett.* **71**, 4154 (1993); D. Rioux, M. Chander, Y. Z. Li, J. H. Weaver, *Phys. Rev. B* **49**, 11071 (1994).
13. H. Brune *et al.*, *J. Chem. Phys.* **99**, 2128 (1993).
14. We thank E. Carter for insightful discussions. This work was supported by the National Science Foundation (grant DMR 9307259), the Air Force Office of Scientific Research (grant F496209410075), and the Packard Foundation.

9 August 1994; accepted 10 November 1994

Absorption of Solar Radiation by Clouds: Observations Versus Models

R. D. Cess, M. H. Zhang, P. Minnis, L. Corsetti, E. G. Dutton, B. W. Forgan, D. P. Garber, W. L. Gates, J. J. Hack, E. F. Harrison, X. Jing, J. T. Kiehl, C. N. Long, J.-J. Morcrette, G. L. Potter, V. Ramanathan, B. Subasilar, C. H. Whitlock, D. F. Young, Y. Zhou

There has been a long history of unexplained anomalous absorption of solar radiation by clouds. Collocated satellite and surface measurements of solar radiation at five geographically diverse locations showed significant solar absorption by clouds, resulting in about 25 watts per square meter more global-mean absorption by the cloudy atmosphere than predicted by theoretical models. It has often been suggested that tropospheric aerosols could increase cloud absorption. But these aerosols are temporally and spatially heterogeneous, whereas the observed cloud absorption is remarkably invariant with respect to season and location. Although its physical cause is unknown, enhanced cloud absorption substantially alters our understanding of the atmosphere's energy budget.

A companion study herein (*1*) highlights a potential shortcoming in our knowledge of cloud-climate interactions: solar (shortwave) absorption by the cloudy atmosphere is greater than theoretical models predict. This result was based on an analysis of the energy budget of the western Pacific warm pool. Shortwave (SW) cloud forcing (C_s) refers to the difference between cloudy-sky (all-sky) and clear-sky net downward (downward minus upward) SW radiation, either at the top of the atmosphere (TOA) or at the surface. Closure of the energy budget requires that the value for C_s at the surface is 1.5 times greater than that at the TOA. Theoretical cloud radiative transfer models typically produce a ratio near unity (*1*), and for the warm pool this amounts to an underestimate in atmospheric SW absorption by more than 30 W m^{-2}, a substantial discrepancy. This result implies that the clouds absorbed more SW radiation than expected. There has been a long history of unexplained anomalous cloud absorption of uncertain magnitude (*2*).

Here, we describe different measurements that address this problem: collocated satellite (TOA) and surface SW measurements that provide a direct assessment of SW absorption by the cloudy atmosphere. For comparison with the collocated data, we used output from two atmospheric general circulation models (GCMs): the European Centre for Medium-Range Weather Forecasts Model (ECMWF GCM; cycle 36 as used at Lawrence Livermore National Laboratory) and version 2 of the National Center for Atmospheric Research Community Climate Model (CCM2). For both, a Gaussian grid of 2.8° by 2.8° was adopted. Many of the ECMWF GCM results were repeated with a 1.1° by 1.1° grid; no dependence on spatial resolution was noted for this study. Like those in the companion study (*1*), our results show considerable and unexplained cloud SW absorption compared to that in the models.

Satellite-surface measurements were collocated at five different locations (Table 1). At Boulder, Colorado, near-surface measurements were made from upward- and downward-facing pyranometers mounted at the top of the 300-m National Oceanic and Atmospheric Administration (NOAA) Boulder Atmospheric Observatory (BAO) tower, thus providing values for the net downward SW. Two sets of collocated satellite data were used. One (Boulder ERBS) consisted of net downward SW at the TOA as measured by the Earth Radiation Budget Experiment (ERBE) SW scanner on the Earth Radiation Budget Satellite (ERBS), whose orbit has a 57° inclination to the equator and provides a sampling of each local hour angle every 36 days. To avoid the foothills of the Rocky Mountains, we ensured that all measurements were averages of pixels falling within a grid extending 0.3°N, 0.3°S, and 0.7°E of the tower (*3*). The second Boulder data set (Boulder GOES), and that for the Wisconsin pyranometer network, used TOA broadband (0.2- to 5.0-μm) albedos computed with the use of visible channel (0.55 to 0.75 μm) brightness counts from the Geostationary Operational Environmental Satellite (GOES) centered over the BAO tower and over each of the individual pyranometer locations of the Wisconsin network (*4*).

The other sites (including Wisconsin) had only upward-facing pyranometers and so provided data on surface insolation (downward SW) rather than for net downward SW at the surface. The collocations of ERBE pixel data at Barrow, Cape Grim, and American Samoa were similar to those in Boulder, except that pixels were averaged over 1° by 1° grids centered at the pyranometer locations. Because ERBS did not view Barrow, ERBE measurements from NOAA 9 (July 1985 and 1986) and NOAA 10 (July 1987) were used. These satellites had sun-synchronous orbits with equator crossing times of 1430 local time (LT) (NOAA 9) and 0730 LT (NOAA 10). Because of its high latitude, Barrow was viewed several times a day by each satellite. The surface measurements were subject to errors typically associated with commercial pyranometers. But several factors resulted in significant error reductions (*5*), so that the accuracy of the surface measurements was limited primarily by the linearity of the instruments, which is better than about 0.5%.

R. D. Cess, M. H. Zhang, X. Jing, Y. Zhou, Institute for Terrestrial and Planetary Atmospheres, Marine Sciences Research Center, State University of New York, Stony Brook, NY 11794, USA.
P. Minnis, E. F. Harrison, C. H. Whitlock, Atmospheric Sciences Division, NASA Langley Research Center, Hampton, VA 23665, USA.
L. Corsetti, W. L. Gates, G. L. Potter, Program for Climate Model Diagnosis and Intercomparison, Lawrence Livermore National Laboratory, Livermore, CA 94550, USA.
E. G. Dutton, Climate Monitoring and Diagnostics Laboratory, Environmental Research Laboratories–National Oceanic and Atmospheric Association, Boulder, CO 80303, USA.
B. W. Forgan, Bureau of Meteorology, G.P.O. Box 1298K, Melbourne, 3001 Victoria, Australia.
D. P. Garber and D. F. Young, Lockheed Engineering and Science Company, Hampton, VA 23666, USA.
J. J. Hack and J. T. Kiehl, National Center for Atmospheric Research, Boulder, CO 80307, USA.
C. N. Long, Department of Meteorology, Pennsylvania State University, University Park, PA 16802, USA.
J.-J. Morcrette, European Centre for Medium-Range Weather Forecasts, Reading, Berkshire RG29AX, UK.
V. Ramanathan and B. Subasilar, Center for Clouds, Chemistry and Climate, Scripps Institution of Oceanography, University of California at San Diego, La Jolla, CA 92126, USA.